Magneto-Hydrodynamic Flow in Electrolyte Solutions

Mian Qin[1] and Haim H. Bau[2*]
[1]Department of Mechanical Engineering and Applied Mechanics, University of Pennsylvania
[2]Department of Mechanical Engineering and Applied Mechanics, University of Pennsylvania
*Corresponding author: bau@seas.upenn.edu

Abstract: The paper presents and compares two models for simulating magneto-hydrodynamic flow of RedOx electrolyte in a conduit patterned with circular pillars. The first model solves the coupled Nernst-Planck and Navier-Stokes equations subjected to Butler-Volmer electrode kinetics and provides detailed information on ions' concentrations. The second model treats the electrolyte as a conductor, and uses current and momentum conservations. Both models are verified and their predictions are compared. Furthermore, we demonstrate the existence of an optimal pillar diameter that maximizes the electric current's density. The work is relevant to microfluidic systems that utilize magneto-hydrodynamics to move and stir fluids without a need for mechanical pumps and valves and, in particular, to chromatographic columns with infinite length.

Keywords: Magneto-hydrodynamics, ion transfer kinetics, flow around a cylinder, porous media flow, microfluidics, chromatographic separation.

1. Introduction

In recent years, there has been a growing interest in the interaction between ionic currents in electrolyte solutions and magnetic fields. The electric currents transmitted in an electrolyte solution interact with the magnetic field to form Lorentz body forces that, in turn, drive fluid motion. The phenomenon is commonly referred to as magneto-hydrodynamics (**MHD**) and has been utilized to drive and control flows in microfluidic conduits [1] and networks [2] without mechanical pumps and valves, to stir and mix fluids [3], and to enhance mass transfer next to electrodes' surfaces [4,5,6]. Most of the literature pertaining to MHD focuses on liquid metals and ionized gases. The modeling of MHD flow of electrolytes is often more complex than that of liquid metals since the local electric conductivity is a function of the electrolytes' concentration, which depends on the flow field. Nernst-Plank equations for the ions' flux (**NP**) [7], the Navier-Stokes momentum equation (**NS**) [8], and Maxwell's equations for the magnetic field need to be solved concurrently. Additionally, one often needs to consider non-linear electrode kinetics. Fortunately, for electrolytes with low magnetic permittivity and a low magnetic Reynolds number, the determination of the magnetic field can be decoupled from that of the ion concentration, fluid flow, and electric fields.

This paper focuses on a heterogeneous chemical reactor for chromatographic separation ([9, 10]), with a MHD drive. To this end, we consider MHD-driven flow of a RedOx electrolyte in a conduit patterned with a periodic array of pillars (**Fig. 1**). The pillars provide increased surface area for catalytic reactions. A pair of electrodes is deposited along the opposing conduit's walls. By imposing an electric potential difference across the electrodes, electric current is transmitted in the electrolyte solution. This current interacts with the magnetic field to induce fluid motion. The detailed ion distributions and the flow field are computed numerically by solving the coupled NP and NS equations. A one-dimensional, semi-analytical, implicit solution of the current-voltage relation for a RedOx electrolyte is constructed to validate the numerical, finite elements solutions. Based on the quasi-analytic solution, a simplified conductivity model is derived that allows computation of the flow drag coefficient in the conduit without calculating detailed ion distributions. We also use porous-media based methodology to model the flow. In the future, the model will be extended to include heterogeneous reactions at the pillars' surfaces.

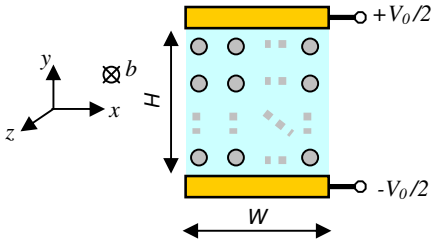

Figure 1: A schematic depiction of a segment of the conduit patterned with a pillar array.

2. Theory

Consider an electrolyte solution subjected to electric and magnetic fields. The concentration

of the i-th species c_i is governed by the NP equation:

$$\frac{\partial c_i}{\partial t} = -\nabla \cdot \vec{N}_i \quad (i=1,....,l), \tag{1}$$

where the mass flux of species i,

$$\vec{N}_i = \vec{u}c_i - D_i \nabla c_i - z_i \nu_i F c_i \nabla \phi, \tag{2}$$

consists of convective, diffusive, and electro-migrative terms. In the above, $\vec{u}$ is the fluid velocity. D_i and $\nu_i = D_i/(RT)$ are, respectively, the diffusivity and the mobility of the i-th species. z_i is the valance of the i-th ion. R is the gas constant. T is the absolute temperature. l is the total number of ion species. F is the Faraday constant. ϕ is the electric potential.

The electric potential satisfies the Poisson equation:

$$-\nabla \cdot (\varepsilon_s \nabla \phi) = F \sum_{k=1}^{N} z_i c_i, \tag{3}$$

where ε_s is the dielectric permittivity of the solvent. We neglect gravity effects. The current flux equals the sum of the ions' net charge flow:

$$\vec{j} = F \sum_{i=1}^{n} z_i \vec{N}_i. \tag{4}$$

The momentum equation is:

$$\rho\left(\frac{\partial \vec{u}}{\partial t} + \vec{u} \cdot \nabla \vec{u}\right) = -\nabla p + \mu \nabla^2 \vec{u} + \vec{f}_{EM}, \tag{5}$$

where the electromagnetic body force

$$\vec{f}_{EM} = \vec{f}_L + \vec{f}_{\nabla B} + \vec{f}_E. \tag{6}$$

In the above, the Lorentz force

$$\vec{f}_L = \vec{j} \times \vec{b}; \tag{7}$$

the magnetophoretic force

$$\vec{f}_{\nabla B} = \frac{\chi_m}{2\varsigma_0} c_i^{(m)} \nabla \vec{b}^2; \tag{8}$$

the electrophoretic force

$$\vec{f}_E = F \nabla \phi \cdot \sum z_i c_i; \tag{9}$$

ρ and μ are, respectively, the fluid density and viscosity; $\vec{b}$ is the magnetic field vector; ς_0 is the magnetic permeability of the vacuum; p is the dynamic pressure; χ_m is the molar susceptibility; and the subscript m denotes paramagnetic ions.

For reversible reactions at the electrodes' surfaces: $Ox + ne^- \Leftrightarrow Red$, the species' fluxes are given by the Butler-Volmer (**BV**) equation [1]:

$$\vec{n} \cdot \vec{N}_{Red} = \frac{j_0}{F}[c_{Ox}/c_{Ox,b} e^{(-\alpha nF/RT)\eta} - c_{Red}/c_{Red,b} e^{[(1-\alpha)nF/RT]\eta}] = -\vec{n} \cdot \vec{N}_{Ox}, \tag{10}$$

where α is the charge transfer coefficient for the cathodic reaction, n is the number of electrons exchanged in the reaction, j_0 is the exchange current's density, $\eta = \phi - V_{ext}$ is the overpotential, c_{Ox} and c_{Red} are, respectively, the concentrations of the oxidized and reduced species at the electrodes' surfaces, and subscript b refers to the bulk of the solution. When multiple reactions take place at the electrodes' surfaces, a separate BV equation is needed for each reacting pair. Solid surfaces, other than electrodes, are impermeable. The boundary conditions (**BC**) associated with the momentum equation consist of no slip at all solid surfaces and zero normal stress at the inlet and outlet. When calculating the flow around the pillar array, we carry out the computations on a unit cell with periodic BCs.

Typically, in a homogeneous solution, net charge exists only in narrow regions next to solid surfaces (electric double layers, **EDL**) and the bulk of the solution is electrically neutral (**EN**):

$$\sum z_i c_i = 0, \tag{11}$$

which leads to zero net total convective flux. The electrophoretic force (equation 9) also vanishes. The current's density when the concentration gradients in the bulk are small is:

$$\vec{j} = -\left(\sum F^2 z_i^2 \nu_i c_i\right) \nabla \phi. \tag{12}$$

The electric current for weakly conducting electrolyte's (when induction is negligible) is:

$$\vec{j} = -\sigma \nabla \phi. \tag{13}$$

The ionic conductivity of the electrolyte solution is:

$$\sigma_{ionic} = \sum F^2 z_i^2 \upsilon_i c_i. \tag{14}$$

Based on a one-dimensional setting, we define the effective conductivity

$$\sigma_{eff} = -jH/\Delta\phi, \tag{15}$$

where H is the distance between the two electrodes, $\Delta\phi$ is the potential drop in the solution's bulk (excluding the two EDLs next to the electrodes' surfaces), and j is the current's density.

Often, based on the Poission (3) and the EN condition (11), researchers conclude $\nabla^2 \phi = 0$.

This is, however, incorrect. Instead, current conservation $\nabla \cdot \vec{j} = 0$ dictates

$$\nabla \cdot (\sigma \nabla \phi) = 0 . \qquad (16)$$

In general, σ is a function of the concentrations and, therefore, depends on space coordinates and time. Equation (16) reduces to the Laplace equation only when the species' concentrations are uniform.

Electrical neutrality exists in the bulk of the solution, but not next to solid surfaces. Typically a surface in contact with aqueous solution acquires net charge, which attracts counterions to form a thin (a few nanometers in thickness) counterion layer (EDL). When the electric field is tangent to the surface, the electrostatic force propels the EDL's ions, which gives rise to electro-osmotic flow. When the device's length scale is much greater than the thickness of the EDL, the flow in the EDL can be approximated by the Smoluchowski slip velocity [11]:

$$u_{//} = -\varepsilon_0 \varepsilon_r \zeta E_{//} / \mu , \qquad (17)$$

where ζ is the difference in potential across the EDL. The subscript // denotes the vector component tangent to the solid/liquid interface. EDLs also exist at the surfaces of the electrodes. We include the effect of the EDLs next to the electrodes in the formulation of the Butler-Volmer equations.

3. Code Verification

To verify the code, we reproduced known results for the drag force associated with a pillar placed mid-distance between two parallel plates and computed the ion distributions in a one-dimensional setting.

3.1 Verification of Flow Simulations

The computational domain spans $x = \pm W/2$ and $y = \pm H/2$. A cylinder of diameter d is centered at the coordinate's origin $(x, y) = (0,0)$. The flow enters the cell with a parabolic velocity profile of maximum velocity u_0 and exits with zero normal stress. The total drag includes both viscous and pressure drag:

$$F_{drag} = F_p + F_\mu = \oint_S \left\{ -n_x p + \mu \left[2 n_x u_x + n_y (u_y + v_x) \right] \right\} dS . \qquad (18)$$

Fig. 2 depicts drag coefficient $\lambda_0 = F_{drag} / (\mu u_0)$ as a function of $\varepsilon = (1-k)/k$, where $k = d/H$. The hollow squares, dotted line, solid line, dots, and dashed line correspond, respectively to our numerical results, Harrison's approximation for $k < 0.4$ [12], Faxen's formula for $k < 0.5$ [13], Ben Richou's numerical results, and the theoretical approximation when $k \to 1$ [14]. Witness the excellent agreement between our finite elements simulation results and literature data.

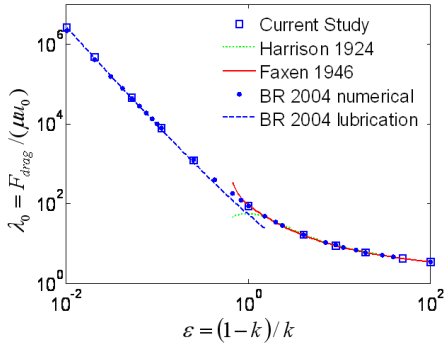

Figure 2: The cylinder's drag coefficient λ_0 as a function of ε. Our finite element simulations (hollow squares); data from [12] (dotted line); data from [13] (solid line); numerical data from [14] (dots); lubrication approximation [14] (dashed line).

3.2 1-D Ion Transport in a DC Field

Consider a RedOx electrolyte consisting of three species $A^{z_1+}, B^{z_2+}, C^{z_3-}$ (e.g., Fe^{3+}, Fe^{2+}, and Cl^-) confined between two parallel electrodes placed distance H apart and subjected to potential difference V_0. The steady state, dimensionless equations (1), (2) and (4) reduce to

$$\begin{aligned} &\frac{dC_1}{dY} + z_1 C_1 \frac{d\Phi}{dY} = -\frac{J}{z_1 - z_2} \\ &\frac{dC_2}{dY} + z_2 C_2 \frac{d\Phi}{dY} = \frac{D_1}{D_2} \cdot \frac{J}{z_1 - z_2} \\ &\frac{dC_3}{dY} - z_3 C_3 \frac{d\Phi}{dY} = 0 \end{aligned} . \qquad (19)$$

In the above, the capital letters denote dimensionless quantities; y, c_i, ϕ and j are, respectively, scaled with H, $\bar{c}_3$, RT/F, and $D_1 F \bar{c}_3 / H$. $\bar{c}_3$ is the average of c_3 and $\bar{c}_1 = g \bar{c}_3$. When $z_1 = 3$, $z_2 = 2$, $z_3 = 1$, and $D_1 / D_2 = 3/4$, one obtains [15]

$$(C_1 + C_2)(3C_1 + 2C_2) = m , \qquad (20)$$

where m is an integration constant. For any g, one can obtain m as a function of J using mass conservation. When $J=0$, $m=(1-g)/2$. It turns out that m is nearly independent of J. Using the Butler-Volmer BCs (10), one obtains an implicit relation of the current as a function of the electrodes' potential difference [16] (**Fig. 3**). The hollow circles, crosses and solid line correspond, respectively, to an exact solution (which does not assume fixed m), an analytic solution that assumes $m=(1-g)/2$, and a finite element solution of the NP equations. Witness the excellent agreement between the finite elements results and the analytic solutions.

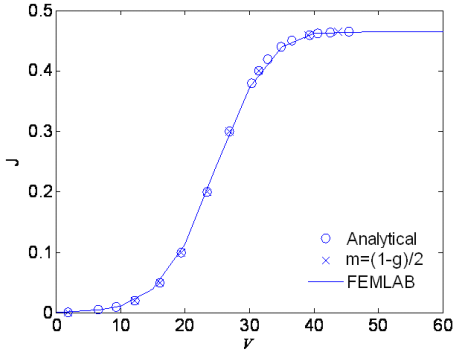

Figure 3: Dimensionless current as a function of the electrodes' potential difference when using exact m values (circles), the approximation $m\sim(1-g)/2$ (crosses), and finite elements (solid line). $\alpha=0.5$. $g=0.2$. $J_0=0.001$.

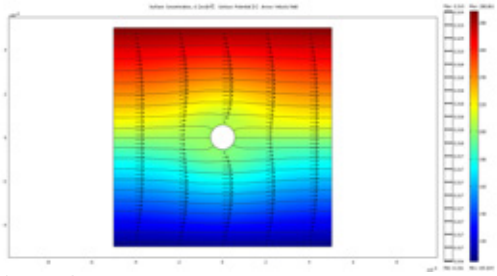

Figure 4: MHD flow around a row of circular pillars confined in a conduit (only one unit cell is shown). The colors describe the concentration distribution of one of the reactive species c_1. The arrows depict the velocity vectors, and the lines are equi-potential lines.

4. MHD Flow in a Conduit Patterned with Pillars

4.1 Mass and Momentum Transport

When pillars are present in the conduit, the convective terms in the NP equation do not vanish, and one needs to solve the coupled NP and NS equations.

First, we study 2-D MHD flow in the presence of a single row of pillars. **Fig. 4** depicts a representative computational cell of height $H=1mm$, width $W=1mm$, pillar's diameter $d=0.11mm$, and periodic BCs at $x=\pm W/2$. $\overline{c}_i=(0.2,0.2,1)M$; $\alpha=0.5$; $j_0=10^{-6}A/m^2$; $B=0.4T$; $V_0=25RT/F$; $z_i=(3,2,-1)$; and $D_i=(1,4/3,1)\times10^{-9}m^2/s$. The figure also shows the flow field (vectors), the equipotential contours (lines) and the concentration of one of the species c_1 (color) when the solid volume fraction $s=\pi d^2/4HW=0.01$.

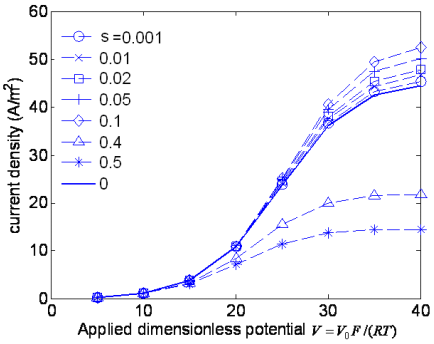

Figure 5: The average current density as a function of the applied dimensionless potential difference V when $s=0$, 0.001, 0.01, 0.02, 0.05, 0.1, 0.4 and 0.5.

Fig. 5 depicts the average current density at the electrode's surface as a function of the dimensionless applied potential ($V=V_0F/RT$) for various solid fractions (s). As V increases, the current initially increases and eventually reaches an asymptotic, limiting value (J_{lim}). Interestingly, when V and the average concentrations are held fixed, as s increases from zero, J_{lim} initially increases, attains a maximum at $s\sim0.1$, and then decreases. The pillar diameter at which the current peaks depends on the potential difference across the electrodes.

Although the pillar blocks some of the cross-sectional area available to current flow and reduces the total number of ions in the conduit, the pillar's presence leads to a vertical velocity component and a stiffer x-velocity gradient next

to the electrode than would have existed in the absence of the pillar. These competing mechanisms modify the concentration field which leads to enhanced current at small s and decreased current at large s. When s is fixed, in the range of parameters studies, the flow rate is linearly proportional to the total current and nearly linearly proportional to the total concentration.

4.2 Ohmic Model

Using the 1-D NP simulations and equation (15), we obtain the effective electric conductivity. $\sigma_{eff} = 8.98\Omega^{-1}m^{-1}$ and $\Delta\phi = 2.64mV$ when $V = 25$. These conductivity and potential difference values are used in all the following ohmic model simulation unless otherwise specified.

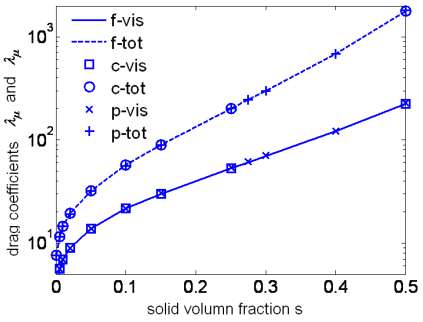

Figure 6: The viscous λ_μ (solid line) and total λ (dashed line) drag coefficient as functions of s. The lines (f), squares/circles (c) and crosses (p) correspond, respectively, to the predictions of the NP, ohmic, and equivalent pressure driven flow models.

We computed the 2-D, MHD flow with the same setup as that in section 4.1 by solving (16) with the NS equation. Fig. 6 compares the results of the NP and ohmic models. The figure depicts the viscous drag coefficient $\lambda_\mu = F_\mu / \mu\bar{u}$ and the total drag coefficient $\lambda = F_{drag} / \mu\bar{u}$, where $\bar{u}$ is the average velocity in the domain. Witness the excellent agreement between both models' predictions. The ohmic model requires much less computational effort than the NP-NS model. The predictions of both models compare well with the drag coefficients computed for pressure-driven flows.

4.3 Multiple Rows of Cylinders

Next, we consider MHD flow in a pillar array with e pillars in each column. The computational domain is sized $H = W = 1mm$. The unit cell consists of a single column of pillars and periodic BCs at $x = \pm W/2$. The vertical distance between adjacent pillars' centers is $h = H/e$. The distances between the top/bottom pillars' centers and the electrodes are $h/2$. We wish to examine the feasibility of obtaining an approximate drag coefficient using a computational cell that consists of a single pillar, symmetry conditions for the velocity field at $y = \pm h/2$, and a potential difference $\Delta\phi/e$ across the cell. The computations utilize the ohmic model.

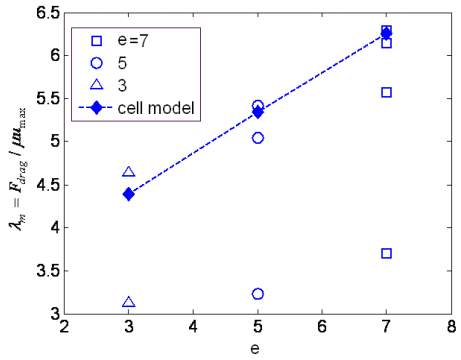

Figure 7: The total drag coefficient λ_m of a pillar as a function of the number of pillars in the column (e). At a particular e value, from top to bottom, the hollow symbols are the drag coefficients for pillars located at $y = 0, \pm h, ..., \pm(e-1)h/2$. The solid diamonds correspond to λ_m calculated with a unit cell consisting of a single pillar.

Fig. 7 depicts the total drag coefficient $\lambda_m = F_{drag} / \mu u_{\max}$ of a pillar centered at $y = 0, h, ..., (e-1)h/2$ as a function of the number of pillars (e) in the column when $e = 3$ (triangles), 5 (circles) and 7 (squares), where $u_{\max}$ is the maximum velocity within the cell. When $e = 7$, the drag coefficients 6.3, 6.1, 5.6, and 3.7 correspond, respectively, to pillars centered at $y = 0, \pm h, \pm 2h$ and $\pm 3h$. The solid diamonds correspond to the drag coefficient calculated using a unit cell with a single pillar. Fig. 7 shows that, the closer the pillars are to the conduit's wall, the lower the drag coefficient. This behavior is due to the drag coefficient being normalized with the maximum velocity in the conduit. When there are many pillars in a column,

the pillars away from the wall experience nearly the same drag coefficient, e.g., when $e=7$, the pillars at position $y=0$ and $\pm h$ have drag coefficients that differ by less than 3%. Thus, when the column consists of a large number of pillars, one can estimate the drag coefficient of most pillars using a computational cell with a single pillar.

4.4 Pillar Array

Next, we consider a conduit populated by many pillars arranged in a square pattern. We use a computational cell sized $H=W=1mm$ and consist of a single pillar (section 4.3).

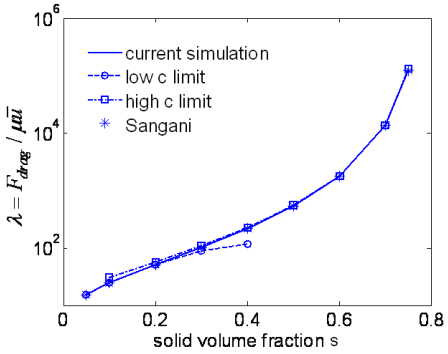

Figure 8: The total drag coefficient λ as a function of s. Finite elements (solid line), asymptotic results for pressure driven flow at small (circles) and large (squares) s [17]; and numerical results for pressure driven flow (stars) [17].

Fig. 8 depicts the drag coefficient λ as a function of s. We compare the drag coefficient of the MHD flow with the drag coefficient of pressure driven flow [17] and obtain excellent agreement. Comparisons of the MHD viscous drag with the pressure-driven drag for other array patterns (not shown here) yielded similar results.

4.5 MHD Flow in Porous Media

Finally, we examine the feasibility of using a porous-media framework to simulate the MHD flow in the pillar array. Creeping flow in a porous medium is often modeled with the Darcy-Brinkman's (DB) equation:

$$\left\{\nabla\cdot\frac{\gamma}{\varepsilon_p}\left[\nabla\bar{u}+(\nabla\bar{u})^T\right]\right\}+\left(\frac{\mu}{\kappa}\bar{u}+\bar{f}_L+\nabla p\right)=0. \quad (21)$$
$$\nabla\cdot\bar{u}=0$$

In the above, $\varepsilon_p=1-s$ is the porosity, $\bar{f}_L$ is the Lorentz body force, and κ (m^2) is the porous medium's permeability. To use equation (21), we need an estimate for the permeability and a model for the electric current distribution. Models for the permeability of various cylinder patterns are available in the literature (i.e., Bruschke [18]). An appropriate model for the electric current is still lacking.

To test the utility of equation (21), we computed the permeability and electric current using a single cell model, with cell size $H=W=0.2mm$, cylinder size $d=0.1mm$, $\Delta\phi=0.264mV$. When $\varepsilon_p=0.8$, we obtain $\kappa=7.96\times10^{-10}m^2$ and $\bar{f}_L=3.19N/m^3$. We used these permeability and body force values for the DB simulation. Then, we solved the MHD equations using a unit cell sized $H=2mm$, $W=0.2mm$ and consist of a column of 10 pillars. $\Delta\phi=2.64mV$. **Fig. 9** depicts the axial velocity profile $u(y)$ at the cell's inlet/outlet as predicted by the MHD ohmic model (dashed line) and the DB model (solid line). The cell-averaged velocities are in excellent agreement with the DB model's predictions. To obtain average quantities, one can significantly reduce the computational effort by using the porous medium model.

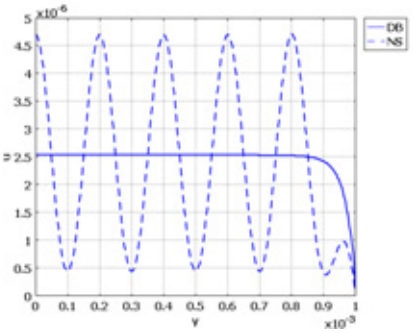

Figure 9: The axial velocity distribution predicted by the MHD ohmic model (dashed line) and the DB model (solid line) for a square pillar array with 10 pillars in each column.

4.6 Slip Flow Effect

Thus far, we have neglected the slip velocity at the surface of the pillars (17). When $B=0.4T$, $\sigma_{eff}=8.98\Omega^{-1}m^{-1}$, $\zeta=50mV$, $\varepsilon_r=80.1$, $\varepsilon_0=8.85\times10^{-12}$ and $H=1mm$, the MHD flow is on the order of $1mm/s$ and the slip velocity is on the order of $0.1\mu m/s$. In other words, the slip velocity is four orders of magnitude smaller than the MHD velocity and can be neglected. Only when the cell size H decreases to tens of

microns, will the slip velocity cause a noticeable change in the velocity field.

5. Conclusions

MHD flow in a conduit patterned with a pillar array was solved using the Nernst-Planck (NP) and Navier-Stokes (NS) equations to obtain the concentrations and the electrical and the velocity fields. The viscous drag coefficient of the MHD flow is in excellent agreement with the drag coefficients predicted for pressure-driven flow around single and multiple pillars.

The NP-NS coupled model is, however, computationally demanding. When one defines an appropriate effective electric conductivity of the medium, the NP equations can be replaced with a simpler, ohmic model, which requires much less computational resources than the NP-NS model. The computational demands can be further reduced by viewing the pillar array as a porous medium and using the Darcy-Brinkman equations to determine average (macroscopic) properties. The paper also examines when the flow in the pillar array can be simulated using computational unit cells with periodic boundary conditions.

Interestingly and counter-intuitively, we find that the presence of pillars in the conduit does not necessarily reduce the current transmitted between the electrodes, which form the conduit's walls. Indeed, small pillars enhance current transmission. We attribute this phenomenon to the modification in the velocity field caused by the pillars, which, in turn, causes modifications in the concentrations' distributions.

References

1. S. Qian and H.H. Bau, Magnetohydrodynamic flow of RedOx electrolyte, *Physics of Fluids*, **17**, 067105 (2005)

2. H.H. Bau, J. Zhu, S. Qian and Y. Xiang, Magnetohydrodynamically controlled fluidic network, *Sensors and Actuators B*, **88**, 205-216 (2003)

3. H.H. Bau, J. Zhong and M. Yi, A minute magneto dydro dynamic (MHD) mixer, *Sensors and Actuators B,* **79***,* 207-215 (2001)

4. A. Alemany and J.P. Chopart, An outline of magnetoelectrochemistry,Magnetohydrodynamic s- Historical Evolution and Trends, *Springer*, 391-407 (2007)

5. O. Lioubashevski, E. Katz and I. Willner, Magnetic force effects on electrochemical processes: A theoretical hydrodynamic model, *Journal of Physical Chemistry B*, **108**, 5778-5784 (2004)

6. N.G.B. Boum, A. Alemany, Numerical simulations of electrochemical mass transfer in electromagnetically forced channel flow, *Electrochemica Acta,* **44**, 1749-1760 (1999)

7. J. Newman, Electrochemical Systems, 2nd ed., *Prentice-Hall*, Englewood Cliffs, NJ (1991)

8. G.K. Batchelor, An Introduction to Fluid Dynamics, *Cambridge University Press* (1967)

9. J.C.T. Eijkel, C. Dalton, C.J. Hayden, J.P.H. Burt and A. Manz, A circular ac magneto-hydrodynamic micropump for chromatographic applications, *Sensors and Actuators B*, **92**, 215-221 (2003)

10. J. Bao and J.D. Harrison, Design and Fabrication of Microchannels for Magneto-hydrodynamic Flow, *Proceedings of the International Conference on MEMS, NANO and Smart Systems* (2003)

11. R.F. Probstein, Physicochemical Hydro-dynamics: An Introduction, *John Wiley & Sons Inc.*, New York, (1994)

12. W.J. Harrison, *Transactions of the Cambridge Philosophical Society*, **23**, 71 (1924)

13. H. Faxen, Forces exerted on a rigid cylinder in a viscous fluid between two parallel fixed planes, *Proc. Roy. Soc. Swedish. Inst. Engrg. Res.*, **187**, 1 (1946)

14. A. Ben Richou, A. Ambari and J.K. Naciri, Drag force on a circular cylinder midway between two parallel plates at very low Reynolds numbers-Part 1: Poiseuille flow (numerical), *Chemical Engineering Science*, **59**, 3215-3222 (2004)

15. A.P. Grigin, Theory of the direct-current flow in Redox systems with one electron transfer reactions, *Russian Journal of electrochemistry,* **29**(9), 938-943 (1993)

16. Y.I. Kharkats, A.V. Sokirko and F.H. Bark, Properties of polarization curves for electrochemical cells described by Butler-Volmer kinetics and arbitrary values of the transfer coefficient. *Electrochemica Acta,* **40**(2), 247-25L (1995)

17. A.S. Sangani and A. Acrivos, Slow flow past periodic arrays of cylinders with application to heat transfer, *Int. J. Multiphase Flow*, **8**, 193-206 (1982)

18. M.V. Bruschke and S.G. Advani, Flow of generalized Newtonian fluids across a periodic array of cylinders, *J. Rheol.,* **37** 479–98 (1993).